ACS APPLIED MATERIALS & INTERFACES

www.acsami.org

Research Article

Lithium Iron Phosphate Enhances the Performance of High-Areal-Capacity Sulfur Composite Cathodes

Xiaosi Gao, Changyang Zheng, Yiqi Shao, Vaidik R. Shah, Shuo Jin, Jin Suntivich,* and Yong Lak Joo*

Cite This: https://doi.org/10.1021/acsami.3c01515

Read Online

ACCESS | Metrics & More | Article Recommendations | Supporting Information

ABSTRACT: Lithium iron phosphate ($LiFePO_4$, "LFP") was investigated as an additive in the cathode of lithium−sulfur (Li−S) batteries. LFP addition boosted the sulfur utilization during Li−S cycling, achieving an initial capacity of 1465 mAh/g_S and a long cycle life (>300 cycles). Polysulfide adsorption experiments showed that LFP attracted polysulfides, and thus, the presence of LFP should alleviate the shuttle effect, a common failure mode. Postmortem characterization found iron phosphides, iron phosphates, and LiF in the electrode, indicating that LFP underwent dynamic reconstruction during Li−S cycling. We suspect that the formation of these species played a role in the observed performance. From the processing standpoint, adding LFP improved slurry rheology, making the preparation of a high-loading electrode more consistent. Benefiting from the high sulfur utilization and the ability to prepare electrodes with high mass loading, the S-LFP hybrid cell showed an excellent areal capacity of 2.65 mAh/cm^2 and could be stably cycled at 2 mAh/cm^2 for 250 cycles. Our results demonstrated the LFP addition as a promising strategy for realizing Li−S batteries with high sulfur loading and areal capacity.

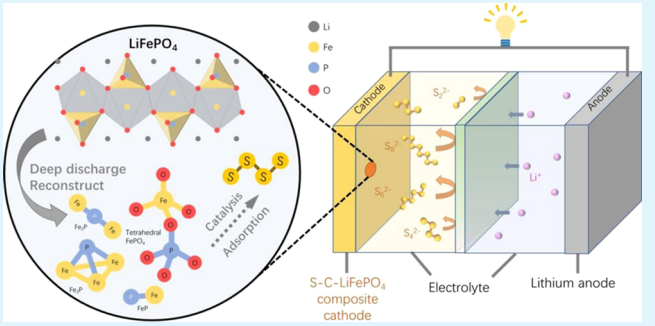

KEYWORDS: *lithium−sulfur batteries, lithium iron phosphate, lithium fluoride, solid−electrolyte interface, cathode−electrolyte interface*

1. INTRODUCTION

Lithium−sulfur (Li−S) batteries are one of the most promising options for beyond lithium-ion batteries (LIBs, ~300 mAh/g), owing to their cost effectiveness and improved gravimetric energy density. Pairing a lithium metal anode (theoretical capacity ~3860 mAh/g_{Li}) to a sulfur composite cathode (theoretical capacity 1672 mAh/g_S)[1] delivers a theoretical specific energy of 2510 Wh/kg, about 10 times of LIB.[2] Meanwhile, sulfur, being the 4th abundant element in the Earth's crust, is more cost-effective than commercial cobalt-based LIBs.[3]

However, Li−S batteries face significant challenges, which limit their commercialization prospect. First, the low conductivity of sulfur (5×10^{-30} S cm^{-1} at 25 °C) restricts their utilization and rate capability.[4] Second, the volume expansion (~80%) from sulfur to its end-of-discharge product Li_2S causes the electrode to lose contact with active sulfur, effectively restricting the sulfur utilization. The common way to address these issues is to use conductive carbon with hollow nanostructures as the cathode;[5,6] however, such an approach reduces the volumetric/areal energy density. Furthermore, the void space inside carbon nanostructures can absorb solvents during the cathode fabrication to negatively impact the slurry rheology. This effect limits the mass loading to often <1 mg/cm^2. This constraint limits the areal capacity of typical Li−S batteries to ~1 mAh/cm^2, lower than 2−3 mAh/cm^2 of LIBs.

Third, Li−S batteries suffer from reactant crossover called the "shuttle effect".[7] During discharge, elemental sulfur (S_8) is reduced to polysulfide (PS, Li_2S_x, x = 4−8) intermediates before forming the end product Li_2S.[8] These polysulfides can dissolve into the electrolyte and spontaneously diffuse to the anode, where they can react with lithium to form insoluble and often insulating species. During charging, the PS can also passivate the lithium anode, leading to capacity loss, self-discharge, and low Columbic efficiency.[9−11] Lastly, the repeated dissolution and deposition between solid sulfur species and polysulfide pose challenges in retaining the sulfur cathode structure over cycling. Re-deposited sulfur may form large insulating clusters ("dead sulfur") that are inactive in the subsequent cycles, leading to active material loss.

Many strategies have been developed in an effort to address the challenges in Li−S batteries. Examples include the use of a stable cathode−electrolyte interface (CEI) to enable uniform sulfur deposition,[12,13] functional interlayers,[14−16] catalysts for polysulfide conversions,[17,18] novel three-dimensional (3D)

Received: February 2, 2023
Accepted: March 31, 2023

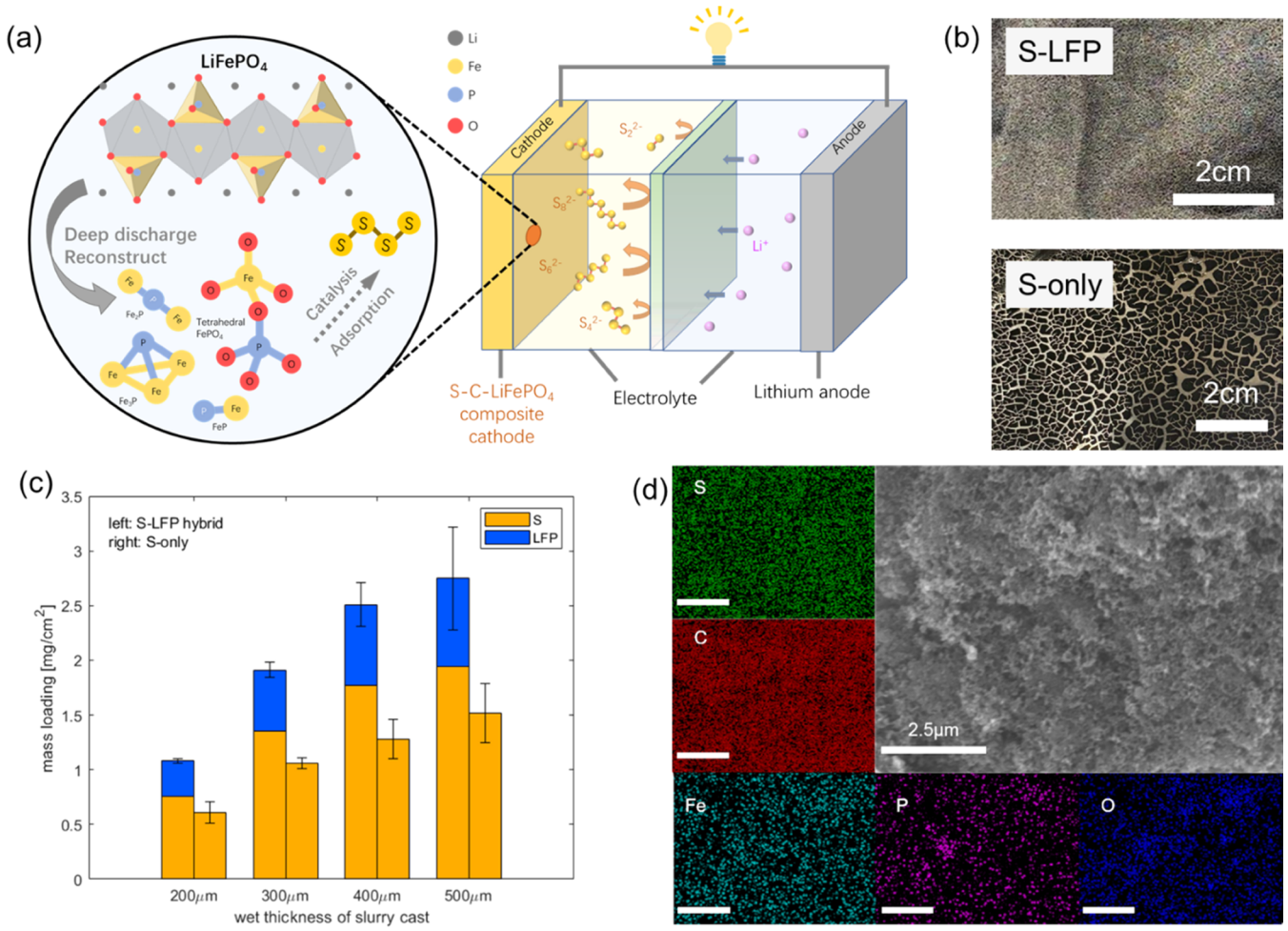

Figure 1. (a) Schematic of LFP reconstruction in Li−S batteries with S-LFP hybrid cathodes. (b) Visual image of the sulfur cathode surface by slurry casting at 400 μm, with and without LFP addition. (c) Average mass loading of sulfur cathodes with and without LFP addition. (d) SEM images of the S-LFP cathode surface and the corresponding EDX (scale bar = 2.5 μm).

host structures,[19,20] and polysulfide adsorbents.[21,22] Chemical compounds have been incorporated into sulfur cathodes as catalytic/adsorptive additives, such as MnO_2,[23] C_3N_4,[9] indium tin oxide (ITO),[24,25] and Co_3S_4.[26] Recently, Li et al. introduced Fe_2P into the sulfur−carbon matrix that provided efficient ion transport and demonstrated strong anchoring of polysulfides, enhancing the specific capacity and rate capability.[27]

Here, we report the use of $LiFePO_4$ as a cathode additive to improve sulfur utilization. $LiFePO_4$ (LFP) is a LIB cathode widely known for its safety and environmental friendliness, but few have studied its potential role as an electrode additive in Li−S batteries. LFP can be partially reduced at the operating potential of Li−S batteries due to Li^+ over-intercalation. Literature suggested that the reduction products could be lithium-deficient tetrahedral iron phosphate ($FePO_4$)[28,29] or iron-phosphide compounds (e.g., Fe_2P).[30,31] We observed the LFP reduction in the Li−S cell and that this process also triggered LiF formation, which provided an in situ protective coating that strengthened the CEI. Importantly, with the addition of LFP, we observed increased sulfur utilization and uniform deposition, which we attribute to the polysulfide adsorption by LFP and Fe_2P. Li−S batteries using our S-LFP hybrid cathode can reach a gravimetric discharge capacity of 1461 mAh/g_S and stably charge−discharge for 300 cycles at 0.4 mA/cm^2. In addition, the inclusion of LFP improved the slurry rheology during cathode fabrication, consequently enabling high mass loading (~2.5 mg/cm^2 of active materials). The combined advantages of high mass loading and high gravimetric capacity allowed the S-LFP hybrid cathode to reach an areal capacity of 2.65 mAh/cm^2 and stably cycled at 2.0 mAh/cm^2 for 250 cycles, approaching the state-of-art LIB performance.

2. RESULTS AND DISCUSSION

2.1. Incorporating $LiFePO_4$ in Li−S Batteries. $LiFePO_4$ was introduced into sulfur cathodes by dry milling LFP powders with pre-infiltrated sulfur-mesoporous carbon (Ketjen Black EC-600JD, "KB"). The ratio of LFP to S/KB was optimized by rate capability tests (Figure S8), yielding 1:3 ratio as the optimum. We will focus on this recipe, which we will refer to as an "S-LFP" hybrid cathode henceforth. The S-LFP cathodes were paired with lithium metal anodes and galvanostatically charged−discharged within 1.8−2.8 V (typical Li−S testing range) for 200 cycles in ether-based electrolytes. Considering that this potential window is well below the redox potential of LFP (~3.4 V vs Li), we expect LFP to be in the reduced state, where it can form a robust LiF-rich cathode−electrolyte interface (CEI). This reduction

https://doi.org/10.1021/acsami.3c01515
ACS Appl. Mater. Interfaces XXXX, XXX, XXX−XXX

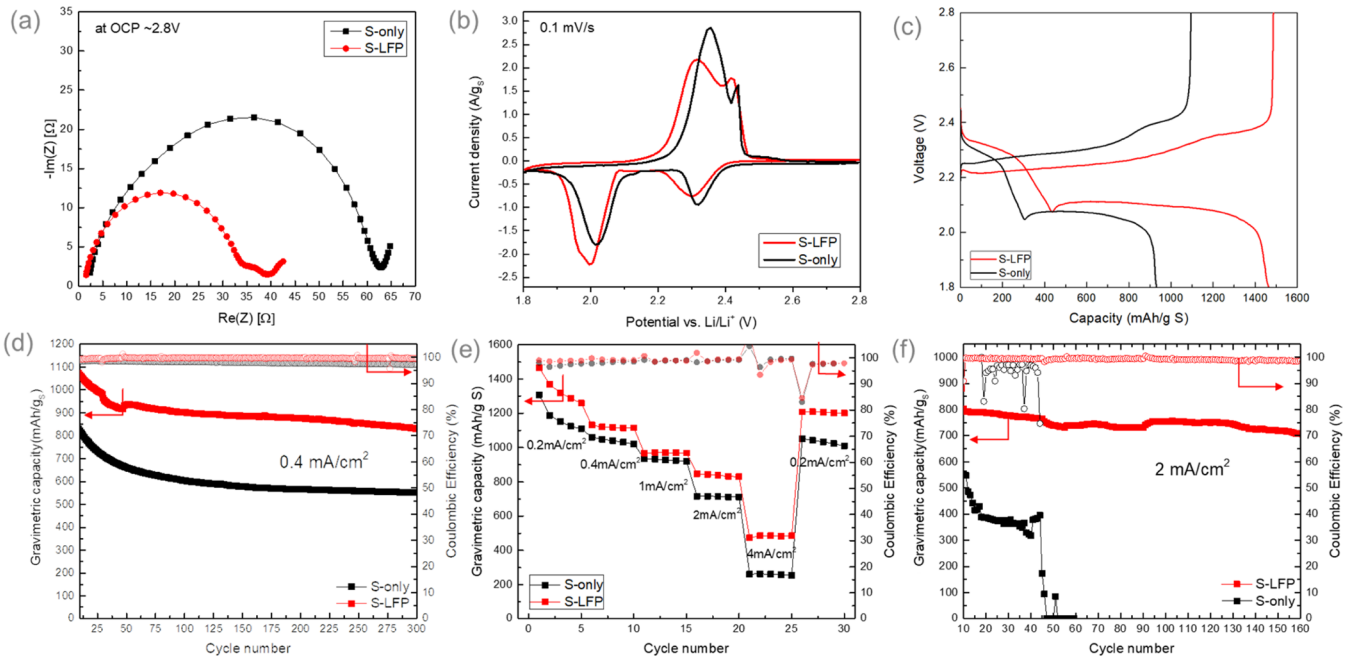

Figure 2. Electrochemical characterizations by gravimetric capacity. (a) EIS, (b) CV, (c) voltage−capacity profile of the first charge−discharge cycle of sulfur cathodes with and without LFP addition. (d, f) Long-term cycling performances of sulfur cathodes with and without LFP at (d) 0.4 mA/cm^2 and (f) 2 mA/cm^2 (omitting the initial formation cycles). (e) Rate capability from 0.2 to 4 mA/cm^2. All capacities were calculated against the sulfur mass.

mechanism is shown schematically in Figure 1a. We will discuss this mechanism in detail in the next section.

Figure 1b shows a representative image of high-loading sulfur cathodes with and without LFP. The presence of LFP improved the slurry rheology, allowing a smooth, dense, and uniform cathode to be reproducibly casted compared to the S-only slurry, which easily cracked. Macroscopic cracking has been a lingering issue for high-loading sulfur cathodes: void spaces in between porous carbon particles take up solvent, causing the carbon matrix to collapse when the solvent evaporates, which leads to cracking when dried. The addition of LFP solved this problem. We attribute this result to the void space reduction, which reduces solvent uptake to preserve the cathode morphology during drying. Effectively, the addition of LFP (~2.2 g/cm^3) improved the packing density of the electrode, increasing the mass loadings at similar volumes (Figures 1c and S10). At a wet thickness of 400 μm (doubling the state-of-the-art thickness protocol), the S-LFP hybrid cathode achieved a high sulfur loading of 1.77 mg$_S$/cm^2, compared to 1.28 mg$_S$/cm^2 without LFP. We also tried other wet thicknesses during slurry casting (Figure 1c). All thicknesses demonstrated ~20 to 30% increase in sulfur mass loading. By further increasing the casting thickness, we could reach 2.41 mg$_S$/cm^2 maximum. Figure 1d shows the surface morphology of S-LFP under scanning electron microscopy (SEM) and energy-dispersive X-ray spectroscopy (EDX) of the same region. From SEM, the surface was smooth and uniform microscopically. From EDX, both the S/KB matrix (S, C) and LFP (Fe, P, O) were well distributed without localized aggregates.

The LFP addition improved the electrochemical performance of the Li−S cells. Electrochemical impedance spectroscopy (EIS, Figure 2a) showed lower impedance at an open-circuit potential (OCP) of ~2.8 V in the fresh S-LFP cell vs S-only cells. The reduced impedance could stem from (1) the LFP filling up the void spaces during slurry casting to create a more interconnected network and (2) the improved electron conductivity (~10^{-6} S cm^{-1} for LFP[32] vs ~10^{-30} S cm^{-1} for sulfur).[4] In Figure 2b, cyclic voltammetry (CV) revealed two redox features at 2.3 V and 2.0 V vs Li/Li$^+$. We assign the first feature (2.3 V vs Li/Li$^+$) to the redox between S_8 and polysulfides and the second feature to the polysulfide conversion to Li_2S/Li_2S_2. Extending the CV to 4.0 V vs Li/Li$^+$ revealed the LFP redox at 3.4/3.6 V vs Li/Li$^+$ (Figure S5), suggesting that LFP did not undergo a charge/discharge process within our 1.8−2.8 V testing range. Figure 2c shows the initial charge/discharge profile of sulfur cathodes with and without LFP. We observed two discharge plateaus at 2.3 and 2.0 V vs Li/Li$^+$, matching the sulfur redox potentials from CV. The S-LFP cathode delivered an excellent gravimetric capacity of 1465 mAh/g$_S$, approaching the theoretical limit of 1651 mAh/g$_S$. This high initial energy density was a result of high sulfur utilization. We will discuss how LFP enabled this ability later.

The capacity improvement was maintained over long-term cycling. Figure 2d demonstrates that the addition of LFP improved long-term capacity retention. At the 300th cycle, the S-LFP cathode delivered 830 mAh/g$_S$ at 99.6% Coulombic efficiency, maintaining 78% of the initial capacity, while only 452 mAh/g$_S$ remained in the S-only cathode at 97.1% Coulombic efficiency, representing 63% of the initial capacity. The superior performance of the S-LFP cathode suggested that less sulfur was lost throughout cycling. As one of the major limitations of the Li−S battery's cycle life, sulfur loss can occur via (1) the shuttle effect as dissolved sulfur species accumulate over cycling and (2) the insulative "dead sulfur" formation created by repeated unregulated deposition of solid S and Li_2S. Adsorption of polysulfides onto LFP and its reduced species can alleviate these issues by ensuring that the sulfur distribution stays on the active area of the electrode to

https://doi.org/10.1021/acsami.3c01515
ACS Appl. Mater. Interfaces XXXX, XXX, XXX−XXX

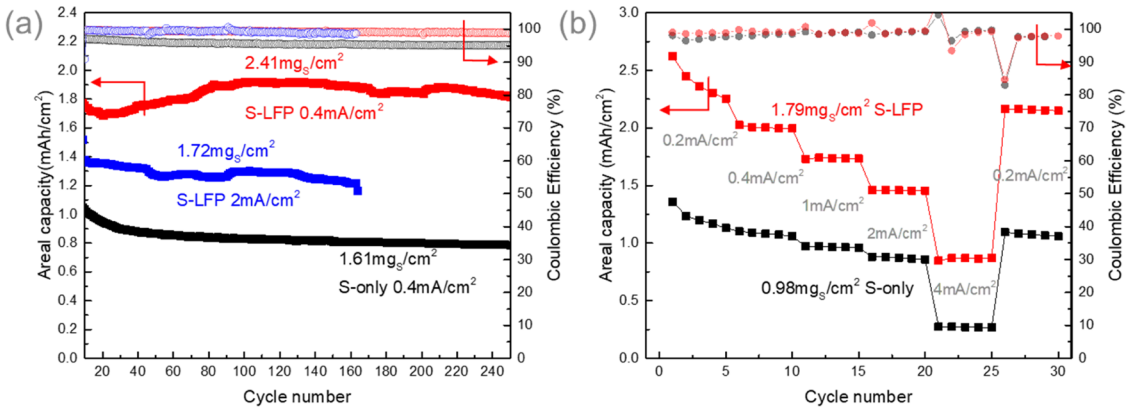

Figure 3. Electrochemical characterizations by areal capacity. (a) Long-term cycling performances of sulfur cathodes with and without LFP at 0.4 and 2 mA/cm^2 (omitting the initial formation cycles). (b) Rate capability from 0.2 to 4 mA/cm^2. All capacities were calculated against the cathode area (15 mm diameter, 1.767 cm^2).

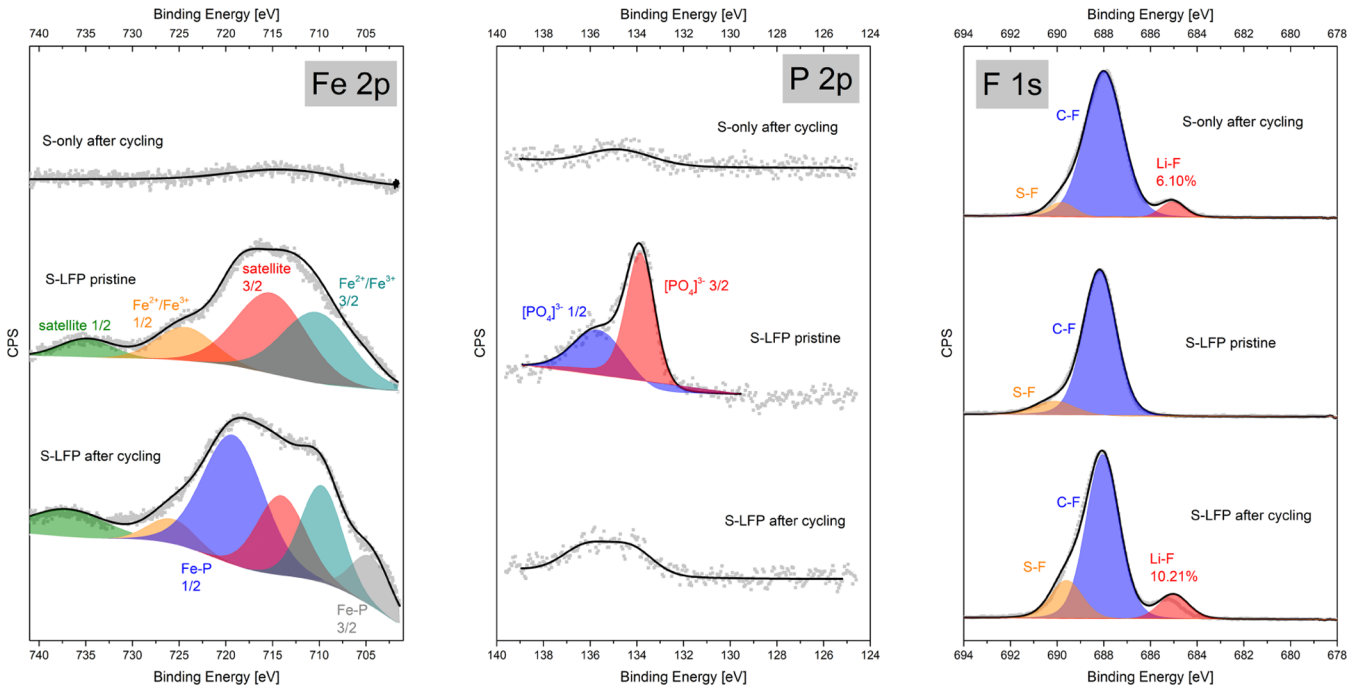

Figure 4. Fe 2p, P 2p, and F 1s XPS scan of the S-LFP hybrid cathode before and after cycling between 1.8−2.8 V.

improve sulfur utilization over cycling. The enhanced capacity retention was additionally supported by the LFP reconstruction upon deep discharge to 1.8 V. The reduction of LFP triggered the formation of lithium fluoride (LiF) in the cathode to form a robust CEI. This stable CEI formation likely enabled a uniform deposition of sulfur species to preserve the cathode structure over cycling and potentially facilitate the conversion between S_8 and Li_2S (i.e., catalysis effect).

The benefits of LFP addition were evident at a high rate. The S-LFP cathode stably delivered 800 mAh/g$_S$ for over 150 cycles at a high current of 2 mA/cm^2 and a significant improvement over 400 mAh/g$_S$ from the S-only cathode, which could only last for less than 50 cycles (Figure 2f). Even at this fast rate, the S-LFP cathode delivered excellent Coulombic efficiency, averaging at 99.1% compared to 96.3% by the S-only cathode. The S-LFP cathode showed improved rate capability over S-only at all currents tested (0.2−4 mA/cm^2, see Figure 2e). The capacity loss after a series of fast charge−discharge cycles was minimal; the S-LFP cathode showed 1209 mAh/g$_S$ at 0.2 mA/cm^2 after being aggressively charged and discharged at 4 mA/cm^2. We hypothesize that similar to regular rate cycling at 0.4 mA/cm^2, LFP benefited the rate capability by suppressing the shuttle effect via polysulfide adsorption and forming a LiF-rich CEI. The improved rate capability may also come from improved conductivity. As we will discuss in the next section, the LFP reduction products (e.g., Fe_2P) can provide additional conductivity through lattice defects.[30,31] The improved conductivity can be observed from Figure S9 that the charge−discharge profile of the first cycle at each rate. Even at a high sulfur loading of 1.79 mg$_S$/cm^2, the S-LFP cathode could still deliver 485 mAh/g$_S$ at 4 mA/cm^2 with two clear discharge plateaus. The lower overpotential/hysteresis was more readily observed in the S-LFP cell than the S-only cell at all rates, indicating the clear benefit of LFP addition.

The increased sulfur mass loading and gravimetric capacity allowed the S-LFP cathode to reach high areal capacity. As discussed above, the LFP addition improved slurry rheology to

https://doi.org/10.1021/acsami.3c01515
ACS Appl. Mater. Interfaces XXXX, XXX, XXX−XXX

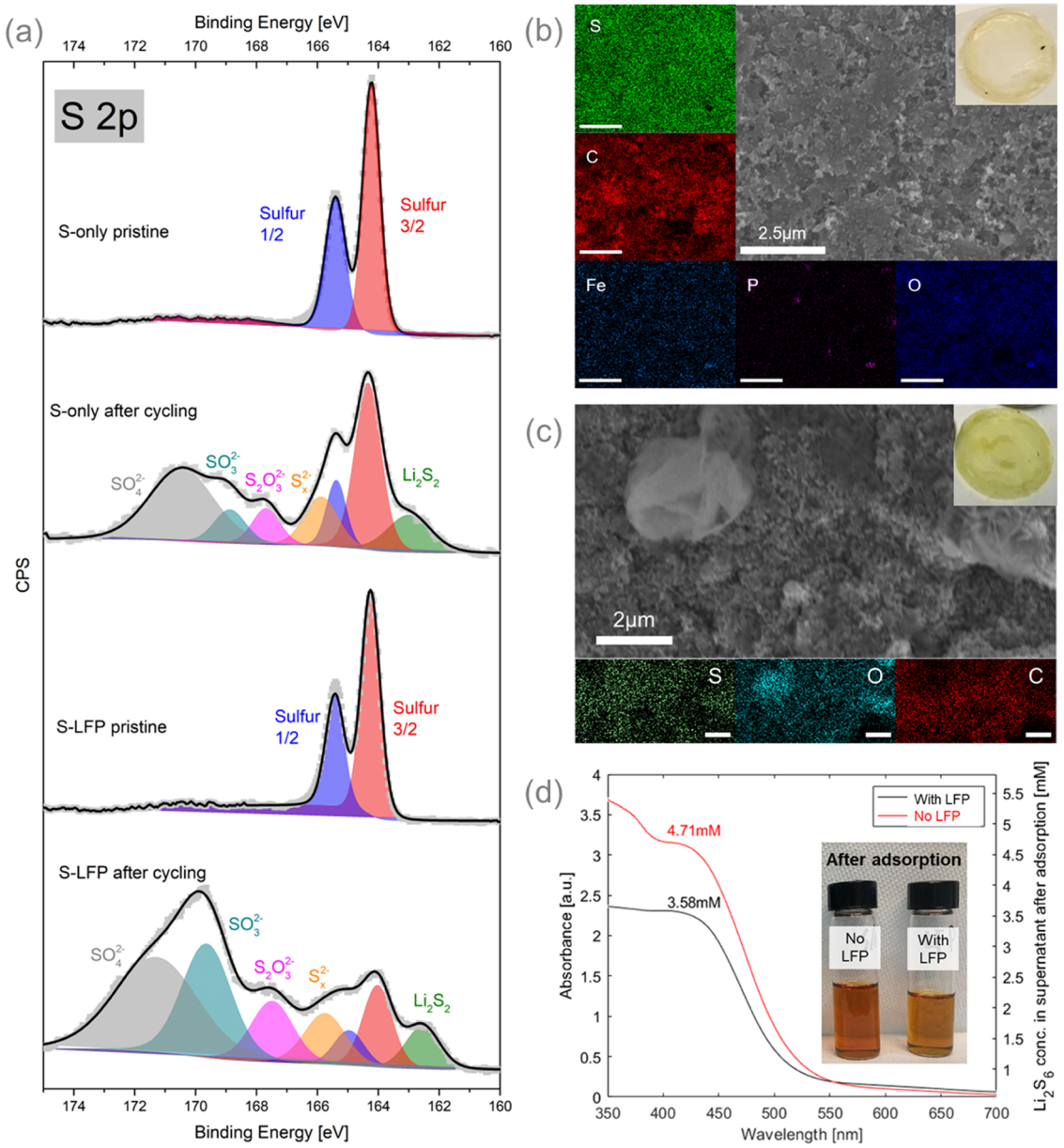

Figure 5. (a) S 2p XPS scan of sulfur cathodes with and without LFP, before and after cycling within 1.8−2.8 V. (b, c) Postmortem SEM and EDX of the (b) S-LFP cathode surface and (c) S-only cathode surface after 200 cycles within 1.8−2.8 V. Inset visual images are separators of the same cells, respectively. (d) UV−vis of remaining Li_2S_6 after adsorption by S-LFP (black) or S-only (red). The initial setup was 20 mg of powder in 5 mM Li_2S_6 in 5 mL of THF. For UV−vis, solutions after adsorption were diluted to < 2 mM to fall within the detection range.

enable high mass loading (up to 2.4 mg_S/cm^2) and created a LiF-rich CEI to increase sulfur utilization. As shown in Figure 3, the high-sulfur-loading cathode (2.41 mg_S/cm^2) delivered a stable areal capacity of 2.0 mAh/cm^2 for over 240 cycles. This performance is at the same level of state-of-the-art Li-ion batteries.[33,34] A slight capacity increase in the initial cycles could be due to the activation of the initial sulfur deposits. Moreover, at a fast charge−discharge rate of 2 mA/cm^2, the S-LFP cell could still maintain 1.4 mAh/cm^2 for 160 cycles. Rate capability test also demonstrated a significantly higher areal capacity at all rates from 0.2 to 4 mA/cm^2, with a maximum of 2.62 mAh/cm^2. Meanwhile, the S-only cathodes suffer from both low loading and limited capacity. The highest loading that our S-only cathode could reach was 1.61 mg_S/cm^2 at which its areal capacity was only 0.8 mAh/cm^2 (Figure 3).

2.2. $LiFePO_4$ Reconstruction upon Deep Discharge.

To reveal how LFP boosted the performance of sulfur cathodes, we performed postmortem X-ray photoelectron spectroscopy (XPS) on the cycled cathodes with and without LFP after 200 cycles at the final discharged state (Figure 4). All binding energies were calibrated against the C−C peak at 284.8 eV of C 1s scan. Expectedly, the Fe 2p and P 2p XPS scan in S-LFP hybrid cathodes had low signals due to low LFP content. The XPS features broadly agree with the XPS results from the LFP-only cathodes (Figures S1 and S2), confirming that LFP was successfully added to the cathode.

Fe 2p XPS contains information on the LFP chemistry. The two peaks at 725.3 and 709.3 eV can be attributed to Fe^{2+}/Fe^{3+} $2p_{1/2}$ and $2p_{3/2}$, respectively, with the accompanying satellites around 736 and 714 eV.[35,36] These peaks are characteristic of the Fe−O bonds in the olivine lattice, consistent to the high-

https://doi.org/10.1021/acsami.3c01515
ACS Appl. Mater. Interfaces XXXX, XXX, XXX−XXX

resolution XPS of LFP nanoparticles by Dedryvère et al.[37] The Fe−O signal decreased after cycling (when referenced to C 1s), suggesting the disruption of Fe−O bonds in the LFP's olivine structure. On the other hand, new Fe $2p_{1/2}$ and $2p_{3/2}$ features appeared at 718.7 and 704.0 eV after cycling. Unfortunately, the $2p_{3/2}$ peak extended beyond the end of the scan at 701 eV, which led to an uncertain baseline and caused the spin−orbit coupling ratio to be off from the theoretical value of 1:2. Judging from the $2p_{1/2}$ peak solely, the most possible identity of this feature was the Fe−P bonds.[38,39] This observation implied that LFP underwent reconstruction by rearranging the Fe−O bond into new species, likely Fe−P structure. Similarly, P 2p XPS suggested the collapse of the LFP structure. The two peaks at 135.6 and 133.8 eV could be ascribed to phosphate $2p_{1/2}$ and $2p_{3/2}$ peaks, respectively, slightly shifted from its published locations of 134.3 and 133.4 eV due to inaccuracies from expanded peak widths at low LFP content.[37,40] Both peaks dropped significantly after cycling, confirming the breakage of P−O bonds in the olivine lattice.

Given the disappearance of the Fe−O and P−O signals and the formation of the Fe−P species, we propose Fe_2P as the reconstruction product in our S-LFP hybrid cathode. The XPS peak position matches the Fe_2P literature values by Nemoshalenko et al. and Kumar et al.,[38,39] as well as our own synthesized Fe_2P (Figure S3). Fe_2P is the side product from the high-temperature LFP calcination,[41] following the disruption of the phosphate tetrahedron (P−O) bonds.[42,43] We hypothesize that the reducing environments may trigger the formation of Fe_2P, specifically, over-discharging LFP to a voltage (1.8 V vs Li/Li^+), which is well below its intercalation redox potential (~3.4 V vs Li/Li^+). Under this condition, over-lithiation may expand and destabilize the olivine lattice, which can degrade to Fe_2P. This proposed pathway has been discussed by Zheng et al.[28] and Shu et al.,[29] whose works found collapsed olivine lattice in LFP samples deep-discharged below 1.5 V, resulting in Fe^{2+} loss ($Li_{1+2x}Fe_{1-x}PO_4$), which eventually turned into non-intercalating tetrahedral $FePO_4$. Lattice destabilization caused by over-lithiation was observed in intercalation-based LIB cathodes, including NMC,[44] MoS,[45] Li_2MoO_3,[46] and $Li_xMn_2O_4$,[47] suggesting that the structural collapse of LFP could occur in an analogous manner. The precise structural identification of the reconstruction product in our hybrid cathode will require additional characterizations but is beyond the scope of this work.

F 1s XPS scan (Figure 4) revealed information on the CEI on the S-LFP cathode. For all cathode samples, the peak at 688.6 eV was assigned to the C−F species, which originated primarily from the PVDF binder[48] and secondarily from the trapped electrolyte salt, LiTFSI.[49] Li−F bond was detected at 685.0 eV[50] after cycling, and the addition of LFP made this feature more prominent than without LFP. The observation suggested that LiF formed as LFP reconstructed. It is known that the reduction of electrolyte salt and solvent can produce LiF in SEI during discharge, as Li^+ catalyzes the $-CF_3$ dissociation from LiTFSI.[51] The LFP reconstruction could provide Li^+ to support localized LiF formation at the cathode. We hypothesize that this LiF formation created a robust CEI to help preserve the structural integrity of the cathode upon repeated dissolution−deposition of sulfur species,[48,52] leading to enhanced Coulombic efficiency and capacity retention[53] as demonstrated in previous sections.

We test the role of deep discharge on the LFP chemistry by measuring XPS of sulfur-free LFP cathodes that have been cycled in two different voltage ranges (1.8−2.8 vs 3−4 V) (Figures S1 and S2). Compared to a regular LFP discharge, which stops at 3 V, deep discharge to 1.8 V led to stronger Fe−P signals and weaker Fe−O and P−O. This finding supports our hypothesis that deep discharge was the cause of the LFP reconstruction in the S-LFP cathode.

2.3. Reducing Dead Sulfur and Shuttle Effect. We characterized the impact of LFP on the sulfur chemistry using XPS S 2p analysis. The doublets at 165.4 and 164.3 eV were ascribed to elemental sulfur $2p_{1/2}$ and $2p_{3/2}$ peaks, respectively (Figure 5a).[54] Various reduction products and intermediates were also identified after cycling, including Li_2S/Li_2S_2 at 162.7 eV, polysulfides (S_x^{2-}) at 165.8 eV, thiosulfates ($S_2O_3^{2-}$) at 167.5 eV, sulfites (SO_3^{2-}) at 169.7 eV, and sulfates (SO_4^{2-}) at 170.8 eV.[55−57] These assignments were based on high-resolution XPS by Fantauzzi et al.[55] Compared to S-only cathodes, more SO_3^{2-} and SO_4^{2-} were observed in the cycled S-LFP cathodes. We suspect that these oxidized sulfur species could develop from the reaction between polysulfides and oxygen species that became available following the collapse of LFP.

Significantly, more elemental sulfur was observed in the cycled S-only cathodes compared to cycled S-LFP cathodes. Considering that our XPS was performed on the fully discharged cathodes at 1.8 V vs Li/Li^+, all sulfur should in theory be in the reduced state, i.e., Li_2S/Li_2S_2. Hence, the detected elemental sulfur was likely electrochemically inactive ("dead") sulfur that was deposited through the shuttle effect. This assignment was further validated by postmortem SEM and EDX analyses of the sulfur cathodes with and without LFP, as shown in Figure 5b,c. A large (>2 μm) particle can be found in the S-only cathode, while the S-LFP cathode remained smooth and uniform under the same magnification. EDX revealed the particle composition to be mainly S and O with very little carbon. Those dead sulfur originated from nonuniform deposition of sulfur and Li_2S during charge and discharge, respectively, which has been discussed in multiple articles.[25,58,59] In our S-LFP cathode, the dead sulfur issue was alleviated by polysulfide adsorption on LFP. Polysulfide adsorption has been proposed to play a significant role in sulfur deposition.[25] Polysulfides can preferentially deposit on surfaces with strong sulfur affinity instead of creating dead sulfur. By avoiding dead sulfur formation, this guided deposition strategy can improve sulfur utilization in Li−S batteries. We believe that LFP is providing this function in our cathode.

To verify the polysulfide adsorption capability of LFP, 20 mg of S/KB powder or LFP powder was dispersed in 5 mM Li_2S_6 solution for > 3 h. We quantified the polysulfide uptake by LFP by measuring the Li_2S_6 remaining in solution by UV−vis (calibration curve in Figure S6). As shown in Figure 5d, less Li_2S_6 was observed in the solution containing LFP both visually and by UV−vis, demonstrating the adsorption capacity of LFP. In addition, Fe_2P, one of the potential degradation products from the LFP reconstruction, has been reported to be a great polysulfide adsorbent.[27] We thus expect the presence of LFP to keep the polysulfides within the cathode and reduce its escape probability to other parts of the cell. A visual comparison between the separators from the S-LFP cell and S-only cell was consistent with this expectation; Figure 5b,c shows that the separator of the S-only cell was significantly darker than the separation from the S-LFP cell, suggesting the presence of polysulfides that have shuttled through the

https://doi.org/10.1021/acsami.3c01515
ACS Appl. Mater. Interfaces XXXX, XXX, XXX−XXX

separator in the S-only situation. Meanwhile, less polysulfides were found on the separator of the S-LFP cell, indicating a reduced shuttle effect.

3. CONCLUSIONS AND OUTLOOK

An introduction of LFP into the sulfur cathode significantly improved the sulfur areal capacity, rate capability, and cycle life. $LiFePO_4$ reconstructed to complex iron-phosphorous-containing compounds (e.g., Fe_2P and other phosphate species) upon deep discharge to the operating potential of Li−S batteries (~1.8 V vs Li/Li^+). This reconstruction developed a LiF-rich CEI that maintained the integrity of the cathode structure over cycling. The result is a Li−S cell with long cycle life up to 300 cycles with excellent rate capability (4 mA/cm^2.) LFP and its reconstruction products alleviate the shuttle effect by adsorbing polysulfides. This adsorption property could help maintain the sulfur deposition on the active area to minimize the formation of dead sulfur clusters upon repeated dissolution and deposition. Finally, the higher electronic conductivity of LFP (and its reconstruction products) could improve the rate capability by reducing the electrode resistance. From the processing standpoint, adding LFP also increased the sulfur mass loading by 20−30% up to 2.41 mg_S/cm^2 without sacrificing gravimetric capacity and cycle life, which significantly increased the areal capacity of the Li−S battery to 2.0 mAh/cm^2, approaching the state-of-the-art Li-ion batteries. Our results suggest that the reconstruction products ($FePO_4$, Fe_2P) once identified could be directly added to the sulfur cathode for even better performance. This approach will not only reduce the dead weight of LFP but also allows the preconditioning of the cell to be more straightforward. Identifying the LFP reconstruction product and mechanism and how it is related to the LiF formation is an important future step to understand how to design additives for high-capacity Li−S batteries.

4. EXPERIMENTAL SECTION

4.1. Materials. 1-Methyl-2-pyrrolidone (NMP), poly(vinylidene fluoride) (PVDF, average MW ~ 534,000), lithium sulfide (Li_2S, 99.98% trace metal basis), 1,2-dimethoxyethane (DOL), 1,3-dimethoxyethane (DME), and bis(trifluoromethane)sulfonimide lithium salt, (LiTFSI, 99.95%) were purchased from Sigma-Aldrich. Timical Super C65 and $LiFePO_4$ powder (LFP, carbon content 1.45%) were purchased from MTI Corp. Sulfur powder (sublimed, 100 mesh, 99.5%) and lithium metal (thickness 750 μm) were purchased from Alfa Aesar. Ketjen Black EC-600JD porous carbon was purchased from Akzo Nobel Functional Chemicals LLC.

4.2. Cathode Fabrication. For sulfur (S)−$LiFePO_4$ (LFP) composite cathodes, sulfur and Ketjen Black (KB) at a mass ratio of 8:2 were homogeneously mixed with a pestle and mortar. The as-obtained precursor was then transferred into a sealed reactor and heated at 155 °C for 12 h to melt-infiltrate into the mesopores of KB. After pre-infiltration, S/KB and LFP were ball milled for 30 min using a Retsch Mixer Mill MM 400 in a hardened stainless-steel jar (about 50 mL full capacity) with several 3 mm stainless-steel balls. For the mass ratio of S/KB vs LFP, we attempted 95:5, 85:15, 75:25, and 50:50 as shown in Figure S8, from which 75:25 was determined to be the best and used in all other characterizations. The S-LFP slurry was prepared by mixing 1.4 g of S-KB/LFP sample, 0.4 g of Super C65, and 0.2 g of PVDF in 10−15 g of NMP. The final content of LFP in the cathode was 17.5%. The S-only reference slurry was prepared similarly with S/KB 80/20 replacing the S/KB-LFP mix. The slurry was mechanically mixed by ball milling at 15 Hz for 2−3 h. The above slurry was cast on an Al foil current collector using an MSK-AFA-III automatic thick film coater, followed by drying in air at room temperature overnight, then in air at 60 °C for 4 h, and storing in a desiccator with humidity <10%. The wet thickness for slurry casting was typically set to 400 μm, leading to an average mass loading of 1.77 mg_S/cm^2. The dried S-LFP composite film was punched into disks of 15 mm in diameter for further electrochemical measurements.

LFP reference cathodes were fabricated by mixing 90 wt % LFP, 5 wt % Super C65, and 5 wt % PVDF in 8−10 g of NMP. Ball milling and slurry casting followed the same protocol, yet the LFP mass loading can reach ~5.3 mg/cm^2 at a wet casting thickness of 300 μm due to its high packing density. After drying in air at room temperature overnight, the slurry was further dried at 110 °C overnight under vacuum.

4.3. Electrochemical Measurements. CR2032-type coin cells were used to evaluate the electrochemical performances of composites. The coin cells were assembled in an argon-filled glovebox (MBraun MB 150B-G) with moisture and oxygen levels below 0.1 ppm. Lithium metal was applied as the anode, and 1:1 DOL/DME with 1 M LiTFSI plus 1 wt % $LiNO_3$ was employed as the electrolyte with an electrolyte-to-sulfur (E/S) ratio. A commercial microporous polypropylene membrane (Celgard 2400) was used as the separator.

The galvanostatic charge−discharge cycling tests were performed between 1.8 and 2.8 V using an Arbin BT2000 battery test system. All cells were rested for 4 hours prior to any electrochemical testing. Current densities were chosen as 0.4 mA/cm^2 (regular cycling, approx. 0.2C) and 2 mA/cm^2 (fast cycling, approx. 1C). Formation steps prior to regular cycling were set as 0.2 mA/cm^2 for five cycles, while those prior to fast cycling were 0.2 mA/cm^2 for two cycles, plus 0.4 mA/cm^2 for two cycles, and plus 1 mA/cm^2 for five cycles. Rate capability test was set as five cycles at 0.2, 0.4, 1, 2, 4, 0.2 mA/cm^2 sequentially. Capacity retentions were calculated against the first cycle after formation steps.

A BioLogic SP-150 potentiostat was employed for cyclic voltammetry (CV) and electrochemical impedance spectrometry (EIS). The CV measurement was carried out at a scan rate of 0.1 mV/s within 1.8−2.8 V. EIS analysis was carried out in a frequency range of 10^6−0.1 Hz. All cycling and electrochemical measurements were conducted at 25 °C.

4.4. Material Characterization. The morphological and microstructure characteristics of the as-fabricated cathodes were investigated by scanning electron microscopy (SEM, Zeiss Gemini 500 FESEM). Elemental mapping analysis was performed by energy-dispersive spectra (EDX) accompanying the Zeiss SEM. A TA Instruments Q500 thermogravimetric analyzer (TGA) was used to ascertain the sulfur and carbon content by scratching off active materials from the S-LFP slurry.

As for postmortem analysis, the fully discharged coin cells after cycling were immediately transferred into an argon-filled glovebox and disassembled. Photos of the separator were taken without any washing or modification. The cathodes were carefully washed in 1:1 DOL/DME to remove the remaining electrolyte and naturally dried in the glovebox. Morphologies of the cycled cathode surfaces were then characterized by the Zeiss SEM, while the elemental composition and chemical bonding information were obtained by XPS on a Scienta Omicron ESCA 2SR X-ray photochemical spectroscope with monochromatic Cu Kα radiation.

4.5. Polysulfide Adsorption Test. 250 mM Li_2S_6 was synthesized by heating stoichiometric Li_2S and S_8 in THF at 80 °C overnight in an argon-filled glovebox. The resulting brown solution was a mixture of polysulfides of various sulfur-chain lengths, with a nominal composition of Li_2S_6. The synthesized Li_2S_6 solution was diluted to 5 mM, and 20 mg of S/KB powder or LFP powder was added and well-mixed. After resting for >3 h, the fully adsorbed powders were removed by 1 and 0.1 μm syringe filters sequentially. The filtered supernatants were sealed in capped quartz cuvettes and immediately analyzed by UV−vis spectroscopy (Agilent Cary 6000i UV−Vis/NIR instrument) within a wavelength range of 800−300 nm. The Li_2S_6 peak was detected around 420 nm. To quantify the Li_2S_6 concentration, UV−vis was performed on a series of known Li_2S_6 concentrations, and the peak intensity at 420 nm was correlated to the concentration by a linear fit (Figure S6).

https://doi.org/10.1021/acsami.3c01515
ACS Appl. Mater. Interfaces XXXX, XXX, XXX−XXX

4.6. Synthesis of Fe_2P. First, 2 g of $Fe(NO_3)_3{\cdot}9H_2O$ and 0.32 g of $(NH_4)_2HPO_4$ were dissolved in water with the help of a few drops of nitric acid. The solution was dried at 80 °C for 4 h in air to yield a clear yellow−orange solid. The solid was then heated to 650 °C for 5 h in H_2 at a ramp rate of 5 °C/min and then naturally cooled to room temperature. The final product was verified by XRD (Figure S3) to be >97% pure Fe_2P.

■ ASSOCIATED CONTENT

Supporting Information

The Supporting Information is available free of charge at https://pubs.acs.org/doi/10.1021/acsami.3c01515.

P 2p, Fe 2p, and F 1s XPS scans of LFP-only cathodes, both in ether-based electrolytes for Li−S batteries and in ether-based electrolytes for LIB; P 2p and Fe 2p XPS scans for self-synthesized Fe2P powders; survey XPS scans; CV within 1.8−4.0 V; UV−vis calibration of Li2S6 solutions; TGA of S-LFP hybrid cathode; rate capability tests of various LFP contents in S-LFP hybrid cathodes; charge−discharge voltage profiles corresponding to the rate capability test; and XRD of synthesized Fe_2P (PDF)

■ AUTHOR INFORMATION

Corresponding Authors

Jin Suntivich − *Department of Materials Science and Engineering, Cornell University, Ithaca, New York 14853, United States*; Email: jsuntivich@cornell.edu

Yong Lak Joo − *Robert Frederick Smith School of Chemical and Biomolecular Engineering, Cornell University, Ithaca, New York 14853, United States*; orcid.org/0000-0002-4646-1625; Email: ylj2@cornell.edu

Authors

Xiaosi Gao − *Robert Frederick Smith School of Chemical and Biomolecular Engineering, Cornell University, Ithaca, New York 14853, United States*

Changyang Zheng − *Department of Materials Science and Engineering, Cornell University, Ithaca, New York 14853, United States*

Yiqi Shao − *Robert Frederick Smith School of Chemical and Biomolecular Engineering, Cornell University, Ithaca, New York 14853, United States*

Vaidik R. Shah − *Robert Frederick Smith School of Chemical and Biomolecular Engineering, Cornell University, Ithaca, New York 14853, United States*

Shuo Jin − *Robert Frederick Smith School of Chemical and Biomolecular Engineering, Cornell University, Ithaca, New York 14853, United States*; orcid.org/0000-0003-0425-9143

Complete contact information is available at: https://pubs.acs.org/10.1021/acsami.3c01515

Author Contributions

This manuscript was written through contributions of all authors. All authors have given approval to the final version of the manuscript.

Funding

This work was funded by the Battery 500 Seedling Program of the Energy Efficiency & Renewable (EERE) Office in US Department of Energy (DE-EE0008193).

Notes

The authors declare no competing financial interest.

■ ACKNOWLEDGMENTS

This work was funded by the Battery 500 Seedling Program of the Energy Efficiency & Renewable (EERE) Office in US Department of Energy (DE-EE0008193). Spectroscopy characterizations made use of the Cornell Center for Materials Research Shared Facilities, which are supported through the NSF MRSEC program (DMR-1719875). The authors also thank Dr. Shuangyan Lang and Dr. Héctor D. Abruña for valuable discussions.

■ REFERENCES

(1) Guo, W.; Zhang, W.; Si, Y.; Wang, D.; Fu, Y.; Manthiram, A. Artificial Dual Solid-Electrolyte Interfaces Based on in Situ Organothiol Transformation in Lithium Sulfur Battery. *Nat. Commun.* **2021**, *12*, No. 3031.

(2) Bruce, P. G.; Freunberger, S. A.; Hardwick, L. J.; Tarascon, J.-M. Li−O 2 and Li−S Batteries with High Energy Storage. *Nat. Mater.* **2012**, *11*, 19−29.

(3) Manthiram, A.; Fu, Y.; Chung, S.-H.; Zu, C.; Su, Y.-S. Rechargeable Lithium−Sulfur Batteries. *Chem. Rev.* **2014**, *114*, 11751−11787.

(4) Lee, B.-J.; Kang, T.-H.; Lee, H.-Y.; Samdani, J. S.; Jung, Y.; Zhang, C.; Yu, Z.; Xu, G.-L.; Cheng, L.; Byun, S.; Lee, Y. M.; Amine, K.; Yu, J.-S. Revisiting the Role of Conductivity and Polarity of Host Materials for Long-Life Lithium−Sulfur Battery. *Adv. Energy Mater.* **2020**, *10*, No. 1903934.

(5) Fu, A.; Wang, C.; Pei, F.; Cui, J.; Fang, X.; Zheng, N. Recent Advances in Hollow Porous Carbon Materials for Lithium−Sulfur Batteries. *Small* **2019**, *15*, No. 1804786.

(6) Liu, T.; Zhang, L.; Cheng, B.; Yu, J. Hollow Carbon Spheres and Their Hybrid Nanomaterials in Electrochemical Energy Storage. *Adv. Energy Mater.* **2019**, *9*, No. 1803900.

(7) Mikhaylik, Y. V.; Akridge, J. R. Polysulfide Shuttle Study in the Li/S Battery System. *J. Electrochem. Soc.* **2004**, *151*, A1969−A1976.

(8) Kumaresan, K.; Mikhaylik, Y.; White, R. E. A Mathematical Model for a Lithium−Sulfur Cell. *J. Electrochem. Soc.* **2008**, *155*, A576−A582.

(9) Pang, Q.; Nazar, L. F. Long-Life and High-Areal-Capacity Li−S Batteries Enabled by a Light-Weight Polar Host with Intrinsic Polysulfide Adsorption. *ACS Nano* **2016**, *10*, 4111−4118.

(10) Evers, S.; Yim, T.; Nazar, L. F. Understanding the Nature of Absorption/Adsorption in Nanoporous Polysulfide Sorbents for the Li−S Battery. *J. Phys. Chem. C* **2012**, *116*, 19653−19658.

(11) Moy, D.; Manivannan, A.; Narayanan, S. R. Direct Measurement of Polysulfide Shuttle Current: A Window into Understanding the Performance of Lithium-Sulfur Cells. *J. Electrochem. Soc.* **2015**, *162*, A1−A7.

(12) Xing, X.; Li, Y.; Wang, X.; Petrova, V.; Liu, H.; Liu, P. Cathode Electrolyte Interface Enabling Stable Li−S Batteries. *Energy Storage Mater.* **2019**, *21*, 474−480.

(13) Chen, X.; Miao, Z.; Zhang, X.; Yuan, L.; Huang, Y.; Li, Z. Optimizing the Operation Strategy of Solid-Conversion Sulfur Cathodes for Achieving High Total Capacity Contribution throughout the Lifespan. *J. Power Sources* **2022**, *543*, No. 231837.

(14) Su, Y.-S.; Manthiram, A. Lithium−Sulphur Batteries with a Microporous Carbon Paper as a Bifunctional Interlayer. *Nat. Commun.* **2012**, *3*, No. 1166.

(15) Ma, G.; Wen, Z.; Jin, J.; Wu, M.; Wu, X.; Zhang, J. Enhanced Cycle Performance of Li−S Battery with a Polypyrrole Functional Interlayer. *J. Power Sources* **2014**, *267*, 542−546.

(16) Park, D.; Park, S.; Kim, D.-W. Electrospun-Cellulose Derived Free-Standing Carbon Nanofibers as Lightweight, Ultrathin, and Stackable Interlayers for Lithium-Sulfur Batteries. *Chem. Eng. J.* **2021**, *405*, No. 126596.

(17) Li, J.; Niu, Z.; Guo, C.; Li, M.; Bao, W. Catalyzing the Polysulfide Conversion for Promoting Lithium Sulfur Battery Performances: A Review. *J. Energy Chem.* **2021**, *54*, 434−451.
(18) Liu, D.; Zhang, C.; Zhou, G.; Lv, W.; Ling, G.; Zhi, L.; Yang, Q.-H. Catalytic Effects in Lithium−Sulfur Batteries: Promoted Sulfur Transformation and Reduced Shuttle Effect. *Adv. Sci.* **2018**, *5*, No. 1700270.
(19) Ji, X.; Liu, D.-Y.; Prendiville, D. G.; Zhang, Y.; Liu, X.; Stucky, G. D. Spatially Heterogeneous Carbon-Fiber Papers as Surface Dendrite-Free Current Collectors for Lithium Deposition. *Nano Today* **2012**, *7*, 10−20.
(20) Zhao, Y.; Wu, W.; Li, J.; Xu, Z.; Guan, L. Encapsulating MWNTs into Hollow Porous Carbon Nanotubes: A Tube-in-Tube Carbon Nanostructure for High-Performance Lithium-Sulfur Batteries. *Adv. Mater.* **2014**, *26*, 5113−5118.
(21) Liu, J.; Yuan, L.; Yuan, K.; Li, Z.; Hao, Z.; Xiang, J.; Huang, Y. SnO2 as a High-Efficiency Polysulfide Trap in Lithium−Sulfur Batteries. *Nanoscale* **2016**, *8*, 13638−13645.
(22) Song, J.; Gordin, M. L.; Xu, T.; Chen, S.; Yu, Z.; Sohn, H.; Lu, J.; Ren, Y.; Duan, Y.; Wang, D. Strong Lithium Polysulfide Chemisorption on Electroactive Sites of Nitrogen-Doped Carbon Composites For High-Performance Lithium−Sulfur Battery Cathodes. *Angew. Chem., Int. Ed.* **2015**, *54*, 4325−4329.
(23) Liang, X.; Nazar, L. F. In Situ Reactive Assembly of Scalable Core−Shell Sulfur−MnO2 Composite Cathodes. *ACS Nano* **2016**, *10*, 4192−4198.
(24) Tao, X.; Wang, J.; Ying, Z.; Cai, Q.; Zheng, G.; Gan, Y.; Huang, H.; Xia, Y.; Liang, C.; Zhang, W.; Cui, Y. Strong Sulfur Binding with Conducting Magnéli-Phase TinO2n−1 Nanomaterials for Improving Lithium−Sulfur Batteries. *Nano Lett.* **2014**, *14*, 5288−5294.
(25) Yao, H.; Zheng, G.; Hsu, P.-C.; Kong, D.; Cha, J. J.; Li, W.; Seh, Z. W.; McDowell, M. T.; Yan, K.; Liang, Z.; Narasimhan, V. K.; Cui, Y. Improving Lithium−Sulphur Batteries through Spatial Control of Sulphur Species Deposition on a Hybrid Electrode Surface. *Nat. Commun.* **2014**, *5*, No. 3943.
(26) Pu, J.; Shen, Z.; Zheng, J.; Wu, W.; Zhu, C.; Zhou, Q.; Zhang, H.; Pan, F. Multifunctional Co3S4@sulfur Nanotubes for Enhanced Lithium-Sulfur Battery Performance. *Nano Energy* **2017**, *37*, 7−14.
(27) Li, Y.; Lei, X.; Yuan, Y.; Wu, S.; Han, B.; Liu, X.; Liu, W.; Hu, J.; Yang, C.; Lin, Z.; Lu, J. Fe2P-Decorated N,P Codoped Carbon Synthesized via Direct Biological Recycling for Endurable Sulfur Encapsulation. *ACS Cent. Sci.* **2020**, *6*, 1827−1834.
(28) Zheng, Y.; Qian, K.; Luo, D.; Li, Y.; Lu, Q.; Li, B.; He, Y.-B.; Wang, X.; Li, J.; Kang, F. Influence of Over-Discharge on the Lifetime and Performance of LiFePO4/Graphite Batteries. *RSC Adv.* **2016**, *6*, 30474−30483.
(29) Shu, J.; Shui, M.; Xu, D.; Wang, D.; Ren, Y.; Gao, S. A Comparative Study of Overdischarge Behaviors of Cathode Materials for Lithium-Ion Batteries. *J. Solid State Electrochem.* **2012**, *16*, 819−824.
(30) Kim, C. W.; Park, J. S.; Lee, K. S. Effect of Fe2P on the Electron Conductivity and Electrochemical Performance of LiFePO4 Synthesized by Mechanical Alloying Using Fe3+ Raw Material. *J. Power Sources* **2006**, *163*, 144−150.
(31) Herle, P. S.; Ellis, B.; Coombs, N.; Nazar, L. F. Nano-Network Electronic Conduction in Iron and Nickel Olivine Phosphates. *Nat. Mater.* **2004**, *3*, 147−152.
(32) Abhilash, K. P.; Selvin, P. C.; Nalini, B.; Xia, H.; Adams, S.; Reddy, M. V. Electrochemical Analysis of the Carbon-Encapsulated Lithium Iron Phosphate Nanochains and Their High-Temperature Conductivity Profiles. *ACS Omega* **2018**, *3*, 6446−6455.
(33) Park, S.-H.; King, P. J.; Tian, R.; Boland, C. S.; Coelho, J.; Zhang, John C.; McBean, P.; McEvoy, N.; Kremer, M. P.; Daly, D.; Coleman, J. N.; Nicolosi, V. High Areal Capacity Battery Electrodes Enabled by Segregated Nanotube Networks. *Nat Energy* **2019**, *4*, 560−567.
(34) Li, Y.; Yan, K.; Lee, H.-W.; Lu, Z.; Liu, N.; Cui, Y. Growth of Conformal Graphene Cages on Micrometre-Sized Silicon Particles as Stable Battery Anodes. *Nat. Energy* **2016**, *1*, No. 15029.
(35) Castro, L.; Dedryvère, R.; Ledeuil, J.-B.; Bréger, J.; Tessier, C.; Gonbeau, D. Aging Mechanisms of LiFePO4 // Graphite Cells Studied by XPS: Redox Reaction and Electrode/Electrolyte Interfaces. *J. Electrochem. Soc.* **2012**, *159*, A357−A363.
(36) Carraro, G.; Barreca, D.; Bekermann, D.; Montini, T.; Gasparotto, A.; Gombac, V.; Maccato, C.; Fornasiero, P. Supported F-Doped Alpha-Fe2O3 Nanomaterials: Synthesis, Characterization and Photo-Assisted H2 Production. *J. Nanosci. Nanotechnol.* **2013**, *13*, 4962−4968.
(37) Dedryvère, R.; Maccario, M.; Croguennec, L.; Le Cras, F.; Delmas, C.; Gonbeau, D. X-Ray Photoelectron Spectroscopy Investigations of Carbon-Coated LixFePO4 Materials. *Chem. Mater.* **2008**, *20*, 7164−7170.
(38) Nemoshalenko, V. V.; Didyk, V. V.; Krivitskii, V. P.; Senekevich, A. I. Investigation of the Atomic Charges in Iron, Cobalt and Nickel Phosphides. *Zh. Neorg. Khim.* **1983**, *28*, 2182−2192.
(39) Kumar, A.; Bui, V. Q.; Lee, J.; Jadhav, A. R.; Hwang, Y.; Kim, M. G.; Kawazoe, Y.; Lee, H. Modulating Interfacial Charge Density of NiP2−FeP2 via Coupling with Metallic Cu for Accelerating Alkaline Hydrogen Evolution. *ACS Energy Lett.* **2021**, *6*, 354−363.
(40) Wang, B.; Liu, J.; Sun, Q.; Li, R.; Sham, T.-K.; Sun, X. Atomic Layer Deposition of Lithium Phosphates as Solid-State Electrolytes for All-Solid-State Microbatteries. *Nanotechnology* **2014**, *25*, No. 504007.
(41) Chung, S.-Y.; Bloking, J. T.; Chiang, Y.-M. Electronically Conductive Phospho-Olivines as Lithium Storage Electrodes. *Nat. Mater.* **2002**, *1*, 123−128.
(42) Xu, Y.; Lu, Y.; Yan, L.; Yang, Z.; Yang, R. Synthesis and Effect of Forming Fe2P Phase on the Physics and Electrochemical Properties of LiFePO4/C Materials. *J. Power Sources* **2006**, *160*, 570−576.
(43) Ma, Y.; Liu, D. Study on the Impact of Fe2P Phase on the Electrochemical Performance of LiFePO4. *Sci. Eng. Compos. Mater.* **2017**, *24*, 23−27.
(44) Bach, T. C.; Schuster, S. F.; Fleder, E.; Müller, J.; Brand, M. J.; Lorrmann, H.; Jossen, A.; Sextl, G. Nonlinear Aging of Cylindrical Lithium-Ion Cells Linked to Heterogeneous Compression. *J. Energy Storage* **2016**, *5*, 212−223.
(45) Lattice-distorted lithiation behavior of a square phase Janus MoSSe monolayer for electrode applications - Nanoscale Advances (RSC Publishing). https://pubs.rsc.org/en/Content/ArticleLanding/2021/NA/D1NA00112D (accessed June 01, 2022).
(46) Zhou, Y.-N.; Ma, J.; Hu, E.; Yu, X.; Gu, L.; Nam, K.-W.; Chen, L.; Wang, Z.; Yang, X.-Q. Tuning Charge−Discharge Induced Unit Cell Breathing in Layer-Structured Cathode Materials for Lithium-Ion Batteries. *Nat. Commun.* **2014**, *5*, No. 5381.
(47) Yang, X. Q.; Sun, X.; Lee, S. J.; McBreen, J.; Mukerjee, S.; Daroux, M. L.; Xing, X. K. In Situ Synchrotron X-Ray Diffraction Studies of the Phase Transitions in Li x Mn2 O 4 Cathode Materials. *Electrochem. Solid-State Lett.* **1999**, *2*, No. 157.
(48) Zhao, E.; Borodin, O.; Gao, X.; Lei, D.; Xiao, Y.; Ren, X.; Fu, W.; Magasinski, A.; Turcheniuk, K.; Yushin, G. Lithium−Iron (III) Fluoride Battery with Double Surface Protection. *Adv. Energy Mater.* **2018**, *8*, No. 1800721.
(49) Shutthanandan, V.; Nandasiri, M.; Zheng, J.; Engelhard, M. H.; Xu, W.; Thevuthasan, S.; Murugesan, V. Applications of XPS in the Characterization of Battery Materials. *J. Electron Spectrosc. Relat. Phenom.* **2019**, *231*, 2−10.
(50) Leroy, S.; Blanchard, F.; Dedryvère, R.; Martinez, H.; Carré, B.; Lemordant, D.; Gonbeau, D. Surface Film Formation on a Graphite Electrode in Li-Ion Batteries: AFM and XPS Study. *Surf. Interface Anal.* **2005**, *37*, 773−781.
(51) Wang, M.; Huai, L.; Hu, G.; Yang, S.; Ren, F.; Wang, S.; Zhang, Z.; Chen, Z.; Peng, Z.; Shen, C.; Wang, D. Effect of LiFSI Concentrations To Form Thickness- and Modulus-Controlled SEI Layers on Lithium Metal Anodes. *J. Phys. Chem. C* **2018**, *122*, 9825−9834.
(52) Xu, M.; Tsiouvaras, N.; Garsuch, A.; Gasteiger, H. A.; Lucht, B. L. Generation of Cathode Passivation Films via Oxidation of Lithium

https://doi.org/10.1021/acsami.3c01515
ACS Appl. Mater. Interfaces XXXX, XXX, XXX−XXX

Bis(Oxalato) Borate on High Voltage Spinel (LiNi0.5Mn1.5O4). *J. Phys. Chem. C* **2014**, *118*, 7363−7368.
(53) Yildirim, H.; Kinaci, A.; Chan, M. K. Y.; Greeley, J. P. First-Principles Analysis of Defect Thermodynamics and Ion Transport in Inorganic SEI Compounds: LiF and NaF. *ACS Appl. Mater. Interfaces* **2015**, *7*, 18985−18996.
(54) Pang, B.; Köhler, R.; Roddatis, V.; Liu, H.; Wang, X.; Viöl, W.; Zhang, K. One-Step Synthesis of Quadrilateral-Shaped Silver Nanoplates with Lamellar Structures Tuned by Amylopectin Derivatives. *ACS Omega* **2018**, *3*, 6841−6848.
(55) Fantauzzi, M.; Elsener, B.; Atzei, D.; Rigoldi, A.; Rossi, A. Exploiting XPS for the Identification of Sulfides and Polysulfides. *RSC Adv.* **2015**, *5*, 75953−75963.
(56) Lacey, M. J.; Yalamanchili, A.; Maibach, J.; Tengstedt, C.; Edström, K.; Brandell, D. The Li−S Battery: An Investigation of Redox Shuttle and Self-Discharge Behaviour with LiNO3-Containing Electrolytes. *RSC Adv.* **2016**, *6*, 3632−3641.
(57) Xu, X.; Zhou, D.; Qin, X.; Lin, K.; Kang, F.; Li, B.; Shanmukaraj, D.; Rojo, T.; Armand, M.; Wang, G. A Room-Temperature Sodium−Sulfur Battery with High Capacity and Stable Cycling Performance. *Nat. Commun.* **2018**, *9*, No. 3870.
(58) Zheng, J.; Gu, M.; Wang, C.; Zuo, P.; Koech, P. K.; Zhang, J.-G.; Liu, J.; Xiao, J. Controlled Nucleation and Growth Process of Li2S2/Li2S in Lithium-Sulfur Batteries. *J. Electrochem. Soc.* **2013**, *160*, A1992−A1996.
(59) Pan, H.; Chen, J.; Cao, R.; Murugesan, V.; Rajput, N. N.; Han, K. S.; Persson, K.; Estevez, L.; Engelhard, M. H.; Zhang, J.-G.; Mueller, K. T.; Cui, Y.; Shao, Y.; Liu, J. Non-Encapsulation Approach for High-Performance Li−S Batteries through Controlled Nucleation and Growth. *Nat. Energy* **2017**, *2*, 813−820.

https://doi.org/10.1021/acsami.3c01515
ACS Appl. Mater. Interfaces XXXX, XXX, XXX−XXX